

# Electrohydrodynamic deformation and rotation of a particle-coated drop

M. Ouriemi  
IFPEN, Solaize, BP 3 69360, France

P. M. Vlahovska  
School of Engineering, Brown University, Providence, RI, 02912, USA\*  
(Dated: May 14, 2015)

A dielectric drop suspended in conducting liquid and subjected to an uniform electric field deforms into an ellipsoid whose major axis is either perpendicular or tilted (due to Quincke rotation effect) relative to the applied field. We experimentally study the effect of surface-adsorbed colloidal particles on these classic electrohydrodynamic phenomena. We observe that at high surface coverage ( $> 90\%$ ), the electrohydrodynamic flow is suppressed, oblate drop deformation is enhanced, and the threshold for tilt is decreased compared to the particle-free drop. The deformation data are well explained by a capsule model, which assumes that the particle monolayer acts as an elastic interface. The reduction of the threshold field for rotation is likely related to drop asphericity.

PACS numbers:

## I. INTRODUCTION

Electric fields provide a versatile means to control small-scale fluid and particle dynamics, e.g., electrohydrodynamic instabilities for pattern formation in thin polymer films [1–3] or particle suspensions [4], electrohydrodynamic atomization to produce micro- and nanoparticles [5–9], drop and vesicle manipulation [10, 11], and colloidal assembly [12–18]. Fluid interfaces provide additional functionality opening new routes for the bottom-up fabrication of novel structurally complex materials [19–22]. Recent works [23–26] find that micro-particles constrained on a drop surface can form various structures in the presence of applied uniform electric field. The underlying mechanisms are still under investigation but a major driving force in this system is the flow created by the electric shear stresses due to accumulation of charges at the interface.

A particle-free drop placed in an electric field polarizes because of the mismatch of the bulk fluids electrical conductivity,  $\sigma$ , and dielectric constant,  $\epsilon$

$$R = \frac{\sigma_{\text{in}}}{\sigma_{\text{ex}}}, \quad S = \frac{\epsilon_{\text{ex}}}{\epsilon_{\text{in}}}. \quad (1)$$

Upon application of an electric field, mobile charges carried by conduction accumulate at the boundary (even though the net charge on the interface remains zero), see Figure 1. For a sphere placed in a uniform electric field with magnitude  $E_0$ , the induced surface free charge distribution increases as [27, 28]

$$Q = 3\epsilon_{\text{in}}E_0 \frac{1-RS}{R+2} (1 - e^{-t/t_{mw}}) \sin \theta \quad (2)$$

$$t_{mw} = \frac{\epsilon_{\text{in}} + 2\epsilon_{\text{ex}}}{\sigma_{\text{in}} + 2\sigma_{\text{ex}}}.$$

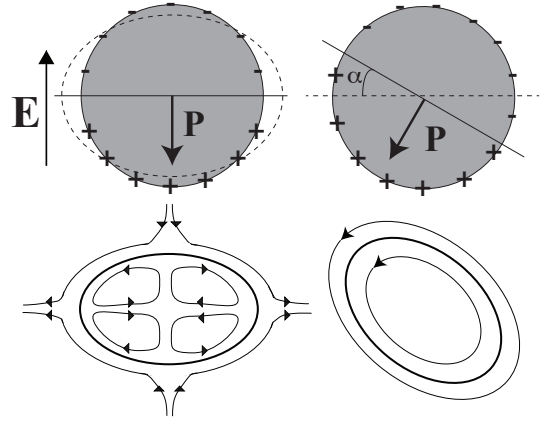


FIG. 1: Drop polarization and electrohydrodynamic flow streamlines for  $RS < 1$  in applied uniform DC electric field. (a) Weak fields with  $E_0 < E_Q$ , where  $E_Q$  is given by Eq. 7, induce pure straining flow and axisymmetric oblate deformation. (b) In strong fields,  $E_0 > E_Q$  constant torque is induced by the misaligned dipole, the flow acquires a rotational component, and the drop is tilted with respect to the applied field direction.

where  $\theta$  is the angle with the applied field direction and  $t_{mw}$  is the Maxwell-Wagner polarization time. The subscripts “in” and “ex” denote the values for drop and suspending medium, respectively. Thus, the polarity of the induced charge is determined by the product of  $R$  and  $S$ , which compares the conduction response of the media [29, 30]. If  $RS < 1$ , the conduction in the drop is slower than the suspending liquid. As a result, the interface charge distribution is dominated by charges brought from the suspending medium and the drop dipole moment is oriented opposite to the applied electric field direction (note that in the opposite case,  $RS > 1$ , the particle dipole is reversed and it is aligned with the electric field.)

The electric field acting on the induced surface charges creates a tangential stress,  $\tau_{r\theta} = QE_\theta$ . In the case of a

\*Electronic address: petia.vlahovska@brown.edu

simple fluid-fluid interface such as oil-water this shear stress can only be balanced by viscous stresses due to fluid flow. In weak fields, for which the electric stresses  $\varepsilon_{\text{ex}} E_0^2$  are smaller than the capillary stress due to surface tension  $\gamma/a$  so that drop shape remains nearly spherical

$$Ca = \frac{a\varepsilon_{\text{ex}} E_0^2}{\gamma} \ll 1, \quad (3)$$

where  $a$  is the drop radius and  $\gamma$  is the interfacial tension, at steady state the fluid undergoes axisymmetric straining flow about the drop [31], see Figure 1.(a), with surface velocity

$$u_\theta = \frac{2\tau_{r\theta}}{1+\lambda} = \frac{9\varepsilon_{\text{in}} E_0^2 (1-RS)}{(1+\lambda)(R+2)^2} \sin(2\theta). \quad (4)$$

where  $\lambda = \mu_{\text{in}}/\mu_{\text{ex}}$  is the viscosity ratio. The charge distribution corresponding to  $RS < 1$ , illustrated in Figure 1.(a), results in surface fluid motion from the pole to the equator and the equator is a stagnation line. Drop deformation resulting from the action of the electric stresses is either oblate or prolate ellipsoid [31]

$$D = \frac{d_{||} - d_{\perp}}{d_{||} + d_{\perp}} = \frac{9Ca}{16S} \Phi(R, S, \lambda), \quad (5)$$

$$\Phi = \frac{1}{(2+R)^2} \left[ S(R^2 + 1) - 2 + 3(RS - 1) \frac{3\lambda + 2}{5\lambda + 5} \right]$$

where  $d_{||}$  and  $d_{\perp}$  are the spheroid axes parallel and perpendicular to the direction of the applied electric field.

Recently it was observed that a nonaxisymmetric rotational flow may appear for drops with  $RS < 1$ , see Figure 1.(b). The drop can assume steady tilted orientation with respect to the electric field direction [32, 33] or oscillate [34, 35]. These behaviors have been linked to the Quincke rotation phenomenon [36–39], which is an instability arising from the unfavorable orientation of the induced dipole (for  $RS < 1$  the dipole direction is opposite to the applied electric field and “wants” to flip). The complete flip of the dipole is prevented by charge supply from the bulk: the induced surface charge (dipole) rotates with the particle, but at the same time the suspending fluid recharges the interface. The balance between charge convection by rotation and supply by conduction from the bulk results in a steady misaligned torque and continuous spinning in the case of a rigid sphere, the so called Quincke rotation. The rotation rate  $\omega$  and the steady oblique dipole orientation, characterized by the angle  $\alpha$  (illustrated in Figure 1.(b)) are

$$\omega = \frac{1}{t_{mw}} \sqrt{\frac{E^2}{E_Q^2} - 1}, \quad \alpha = \text{arccot} \left[ (\omega t_{mw})^{-1} \right] \quad (6)$$

where  $E_Q$  is the threshold electric field above which the rotation occurs and  $t_{mw}$  is the Maxwell-Wagner polarization time

$$E_Q^2 = \frac{2\sigma_{\text{ex}}\mu_{\text{ex}}(R+2)^2}{3\varepsilon_{\text{ex}}\varepsilon_{\text{in}}(1-RS)}, \quad (7)$$

$R$  and  $S$  are the conductivity and permittivity ratios defined by Eq. 1. In the case of drops, the electric torque generates rotational fluid motion [32, 33], in addition to the already present straining flow. The resulting linear flow causes the drop to deform into a general ellipsoid whose major axis is misaligned with the applied electric field. The steady oblique orientation and deformation of the drop were experimentally and theoretically investigated by our group [33, 35, 40].

Given the complex behavior of a drop with a simple fluid interface, a question naturally arises: how does surface modification changes drop electrohydrodynamics? We studied experimentally a microparticle-coated drop with  $RS < 1$  in the Taylor regime (below the threshold for Quincke rotation) and at low to moderate surface coverages (below 50%) [24]. Particles initially randomly distributed at the surface formed a “belt” around the equator as the drop deforms into an oblate shape. This is an expected consequence of the straining electrohydrodynamic flow. In stronger DC fields, the dynamics of these “armored” drops becomes more complex [23, 24] and depends on the particles characteristics. Belts formed by low polarizability particles break into a sequence of counter-rotating vortices of particles. When dipole-dipole attraction becomes strong the particle chain and the drop experiences a prolate deformation and tip-streaming occur with ejection of particles. For non-spherical conductive particles, we have observed drop “kayaking”: its major axis precessing around the applied field direction.

In this work we investigate drops at high particle-coverage. The particle-covered drop is modeled as a capsule and the experimentally measured drop deformation,  $D$ , as a function of field strength,  $Ca$ , is used to find the shear elasticity of particle monolayers. We also investigate the effect of particle coverage on the onset for Quincke rotation, and we find that high surface coverage of particles drastically reduces the critical fields strength of rotation.

## II. EXPERIMENTAL SECTION

### A. Materials

The suspending fluid is castor oil (Alfa Aesar) with viscosity  $\mu_{\text{ex}} = 0.69$  Pa.s, dielectric constant  $\varepsilon_{\text{ex}} = 4.6\varepsilon_0$ , where  $\varepsilon_0$  is the vacuum permittivity, conductivity  $\sigma_{\text{ex}} = 3.8 \times 10^{-11}$  S/m, and density  $\rho_{\text{ex}} = 962$  kg/m<sup>3</sup>. The drop fluid is silicon oil with  $\mu_{\text{in}} = 0.05$  Pa.s,  $\varepsilon_{\text{in}} = 2.8\varepsilon_0$ ,  $\sigma_{\text{in}} = 2.4 \times 10^{-12}$  S/m,  $\rho_{\text{in}} = 963.5$  kg/m<sup>3</sup> (UCT). The surface tension between the castor oil and the Silicone oil is 4.5 mN/m [33]. The permittivity and the conductivity were measured using a dielectric constant meter and a conductivity meter from Scientifica. The viscosity and density are specified by the company-provider. The characteristics of the particles are summarized in Table I.

Shape	Type	density $\rho_p$ ( $kg/m^3$ )	radius $r$ ( $\mu m$ )	Conductivity	Supplier
irregular	Aluminum (Al)	2600	1.5, 12	++	Atlantic equipment
sphere	glass (G)	2200	3.5, 8.5	+	Corpuscular/Cospheric
sphere	polyethylene (Pe)	1000	50	—	Cospheric

TABLE I: Particles characteristics. The symbol + indicates that the particles are slightly more conducting than the fluids, ++ highly more conducting, and — less conducting.

## B. Methods

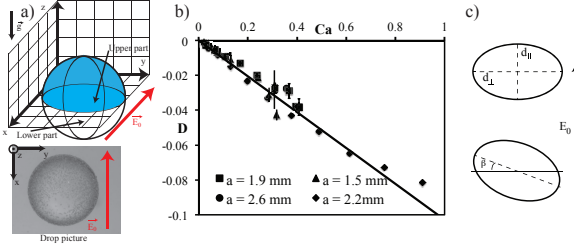


FIG. 2: (a) Drop observation for the experimental measurements. (b)  $D(Ca)$  for a particle-free drop is used to validate the set-up. The symbols are experimental data and the line is the Taylor's theory Eq. 5. (c) Definition of drop deformation and orientation characteristics: the spheroid axes  $d_{||}$  and  $d_{\perp}$  and the tilt  $\beta$ .

The experimental set-up has the same design as the one used in [24]. A uniform DC electric field is created in a parallel-plate chamber made of two 7.6cm by 10.5 cm brass electrodes separated by a gap of 4.5cm. Fields up to 16 kV/cm are generated using a voltage amplifier connected to a DC Power supply. The chamber is filled with castor oil. A drop of silicon oil with suspended micro-particles is injected in the middle of the chamber. The particles are driven to the interface by the application of an electric pulse the duration and strength of which depend on the type of micro-particles; after the field is turned off the particles remain trapped at the interface as the thermal energy is negligible compared to the energy required to remove the particle from the interface. The drop is then manually moved around in order to randomize the particle distribution on the drop surface. In the actual experiment, electric field is applied and drop behavior is recorded for about 3 minutes. On this time scale drop sedimentation is negligible. After each recording, the electrical field is turned off and the drop is moved back to its initial position. This action removes any particle structures. The experiment is repeated for a different electric field strength.

The drop is observed from a direction perpendicular to the field. The top view of the drop is recorded every 0.2s, which is a compromise between memory limitation of the software and the length of the recording. The images are post-processed with ImageJ and Matlab to extract the drop diameter  $d$ , the deformation parameter

$D = (d_{||} - d_{\perp}) / (d_{||} + d_{\perp})$  and the angle  $(\pi/2 - \beta)$  between the drop major axis and the applied field direction, see Figure 2 for definitions. The precision of the measurements is set by the resolution of the pictures; for a drop of radius  $a = 2$  mm it is around 0.0055 mm/px leading to an absolute error in the deformation ( $D$ ) of 0.0045, which decreases for smaller drops. The surface concentration of particles,  $\varphi$ , is defined as the percentage of the drop surface covered by particles (including the space between particles) once the particles are brought together. We measure  $\varphi$  at very low electrical fields,  $E_0 < 60$  kV/m, to minimize particle compaction. The experimental procedure and the material properties are validated by comparing drop deformation with the Taylor model for small deformations[31] given by Eq. 5.

## III. RESULTS

Figure 3 illustrates the typical behaviors of drops with  $\varphi \sim 90\%$  surface coverage. In weak fields, the drop always deforms into an oblate spheroid and the particles accumulate at the equator forming a “belt”. At high coverages, the belt is very wide and only a small region near the poles remains particle free. In stronger fields, the oblate deformation increases and the drops may adopt peculiar “drum-like” shapes. In even stronger fields, the drops may start rotating or implode.

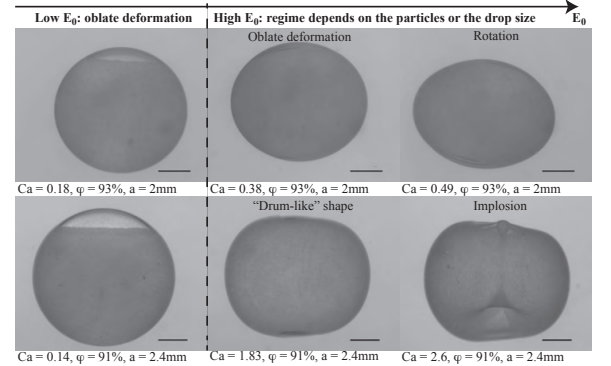


FIG. 3: Typical drop behaviors at high surface coverage of glass spheres (with radius  $r = 8.5 \mu m$ ). The scale bar corresponds to 1 mm.

### A. Weak DC electric fields: increased oblate deformation

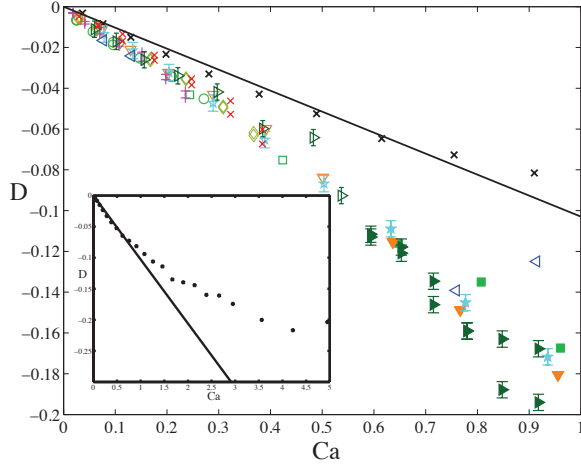


FIG. 4: Drop deformation  $D$  as a function of the dimensionless field strength  $Ca$ . The symbol  $\times$  corresponds to a “clean” (particle-free) drop with radius  $a = 2.2\text{mm}$ , the symbols  $\diamond$ ,  $\square$ ,  $\circ$  and  $\triangle$  denote drops covered with Al ( $r = 12\mu\text{m}$ ) with  $\varphi = 65\%$ ,  $88\%$ ,  $93\%$  and  $96\%$  and  $a = 1.9\text{mm}$ ,  $1.8\text{mm}$ ,  $1.7\text{mm}$  and  $2.2\text{mm}$ , respectively. The symbol  $\star$  corresponds to a drop covered with Al ( $r = 1.5\mu\text{m}$ ) with  $\varphi = 80\%$  and  $a = 2.3\text{mm}$ , the symbol  $\triangleleft$  corresponds to a drop covered with Pe ( $\varphi = 78\%$ ,  $a = 2.2\text{mm}$ ), the symbols  $+$ , and light  $\times$  denote drops covered with G ( $r = 8.5\mu\text{m}$ ) with  $\varphi = 100\%$  and  $93\%$  and  $a = 1.2\text{mm}$ , and  $2\text{mm}$ , the symbol  $\triangleright$  corresponds to a drop covered with G ( $r = 3.5\mu\text{m}$ ) with  $\varphi = 100\%$  and  $a = 1.7\text{mm}$ . The solid line corresponds to the Taylor prediction Eq. 5 for viscosity ratio  $\lambda = 0.07$ . The inset shows the deformation of a particle-free drop in a wider range of  $Ca$ . Filled symbols denote drops in the electrorotation (tilted) regime. For clarity, error bars are shown only for some drops as they are similar for all the measurements.

Figure 4 shows that particle-covered drops undergo larger deformation compared to uncoated (“clean”) drops at the same field strength. Moreover, the magnitude of the deformation is insensitive to particle type, size, and coverage (above  $\varphi = 65\%$ ).

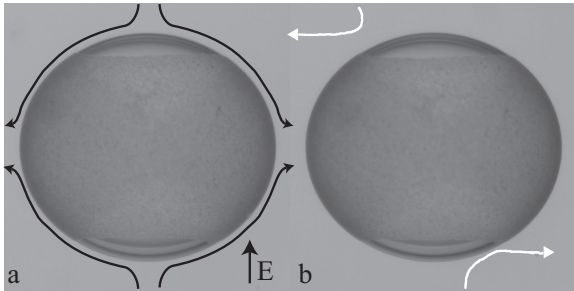


FIG. 5: Streamlines of the flow around a drop. a) Theoretical flow around a clean drop. b) Trajectories measured around a glass covered drop

Once the drop reaches a steady oblate deformation, the particles at the surface do not move, which suggests the absence of electrohydrodynamic flow. To test for

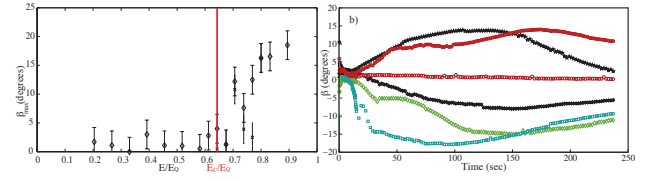


FIG. 6: (a) - Maximum inclination  $\beta_{max}$  measured over 4 minutes as a function of  $E/E_Q$  for a drop covered with G spheres ( $r = 3.5\mu\text{m}$ ). The symbol  $+$  represents the second measurement realized for some  $E/E_Q$ . b- Examples of some temporal evolution of  $\beta$ . The symbol  $\square$  corresponds to  $E/E_Q = 0.89$ , the symbol  $\star$  to  $E/E_Q = 0.70$ , the symbol  $\circ$  to  $E/E_Q = 0.77$ , the symbol  $\diamond$  to  $E/E_Q = 0.80$  and the line to  $E/E_Q = 0.45$ . The filled symbols represent the second measurement realized for some  $E/E_Q$ .

the presence of flow, few large polyethylene spheres (Pe) were used as tracers in the surrounding fluids furnishing a qualitative visualization of the flow around the drop. Figure 5 illustrates the streamlines for the flow around a “clean” drop and the measured trajectories of two particles around a drop covered with glass particles. For high surface coverage, the traces flow from the poles to the belt boundary. Tracers in the vicinity of the surface covered by particles are still. Thus, the presence of particles suppress the electrohydrodynamic flow and limits it to the poles region (‘clean’ portion of the drop).

### B. Stronger DC electrical fields: drop tilt

Particle-covered drops also exhibit Quincke-like (electrorotation) behavior. We find that the inclination angle does increase with field strength, but also exhibits unsteady behavior, see Figure 6. The appearance of nonzero tilt  $\beta$  (steady or unsteady) is defined as the threshold for rotation.

Figure 6.(b) represents the time evolution of the tilt angle  $\beta$  (see Figure 1 for the definition) measured for a drop covered of small glass spheres for different electrical fields. For low electrical fields,  $\beta$  remains nearly zero, i.e., there is no tilt. The small angle is due to errors in the position of the electrical chamber relative to the camera. In stronger field the drop tilts. However, in contrast to ‘clean’ drops which exhibit stationary inclination, the inclination ( $\beta$ ) varies with time, see Figure 6.(b), similarly to the wobbling observed for drops with a low coverage of aluminum particles [24]. time scale of the transients is comparable to the duration of the observation, so we can not conclusively state that the behavior is periodic (e.g., oscillations). Figure 6.(a) represents the maximum inclination  $\beta_{max}$  measured as a function of the electrical fields scaled by the critical value for Quincke rotation ( $E/E_Q$ ). Filled symbols correspond to repeated experiments. Below the rotation threshold,  $E_c/E_Q$ ,  $\beta_{max}$  is within the experimental error;  $E_c$  denotes the critical electric field for the onset of electrorotation in our system (particle-coated drop). Above  $E_c$ ,  $\beta_{max}$  increases with field strength  $E$ . Repeated measurements show that for

a given  $E$ , different inclinations are possible. Finally we observe sometimes that the a drop can spin while having no tilt.

Figure 7.(a) shows the maximum inclination  $\beta_{max}$  measured for drop covered with different particles as a function of  $E/E_Q$ . The scatter of the data suggests that the tilting effect is strongly dependent on particles characteristics. For comparison, the solid black line represents the theoretical dipole orientation prediction for a Quincke sphere Eq. 6 [33].

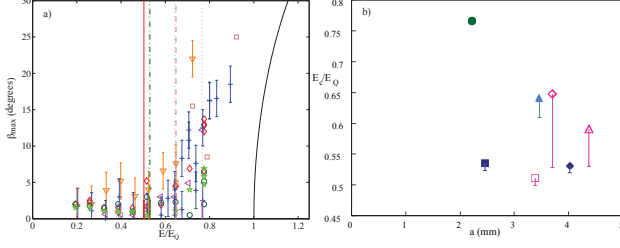


FIG. 7: (a) Maximum inclination  $\beta_{max}$  measured over 4 minutes as a function of  $E/E_Q$ . The vertical lines represent the onset of particle sustained motion for the different drops, and the black thick line represents the prediction for the dipole orientation for a solid particle given by Eq. 6. The symbols  $\diamond$ ,  $\square$ , and  $\nabla$  denote drops covered with Al ( $r = 12\mu\text{m}$ ) with  $\varphi = 93\%$ ,  $88\%$ , and  $96\%$  and  $a = 1.7\text{mm}$ ,  $1.8\text{mm}$ , and  $2.2\text{mm}$ , the symbol  $\blacktriangleleft$  corresponds to a drop covered with Pe ( $\varphi = 78\%$ ,  $a = 2.2\text{mm}$ ), the symbols  $\circ$ , and  $\star$  denote drops covered with G ( $r = 8.5\mu\text{m}$ ) with  $\varphi = 100\%$  and  $93\%$  and  $a = 1.2\text{mm}$ , and  $2\text{mm}$ , the symbol  $+$  corresponds to a drop covered with G ( $r = 3.5\mu\text{m}$ ) with  $\varphi = 100\%$  and  $a = 1.7\text{mm}$ . For clarity, error bars are shown only for some drops as they are similar for all the measurements. (b) Electric field at which sustained drop tilt occurs as a function of the drop diameter. The filled symbol  $\circ$  represents a drop covered with Pe particles for  $\varphi = 78\%$ . The empty symbols represent drops covered with Al particles,  $\diamond$  for  $\varphi = 95\%$ ,  $\square$  for  $\varphi = 93\%$ , and  $\Delta$  for  $\varphi = 88\%$ . The filled  $\Delta$  symbol represents a drop covered with glass sphere ( $r = 3\mu\text{m}$ ) for  $\varphi =$ . The filled  $\square$  and  $\diamond$  symbol represent respectively drops covered with glass spheres ( $r = 12\mu\text{m}$ ) for  $\varphi = 100\%$  and  $\varphi = 94\%$ .

Figure 7.(b) summarizes the threshold fields as a function of the drop diameter for high surface coverage of different types of particles. Independently from the type of particle, the dimensionless critical field strength is in the range  $[0.5-0.8]$ . i.e. two to four times lower than the thresholds measured for “clean” drops and around twice lower than for a solid sphere. Hence, high surface coverage of particles drastically reduces the critical fields strength for onset of rotation.

For very strong electrical fields, the drops exhibit very peculiar behavior, see Figure 8.(a), as drop implosion or bucking of the layer of particles leading to either ejection of cluster of particles similar to the ejection observed for lower surface coverage [24], or the formation of ephemeral dynamic wings. Figure 8.(b) illustrates ephemeral wings formation.

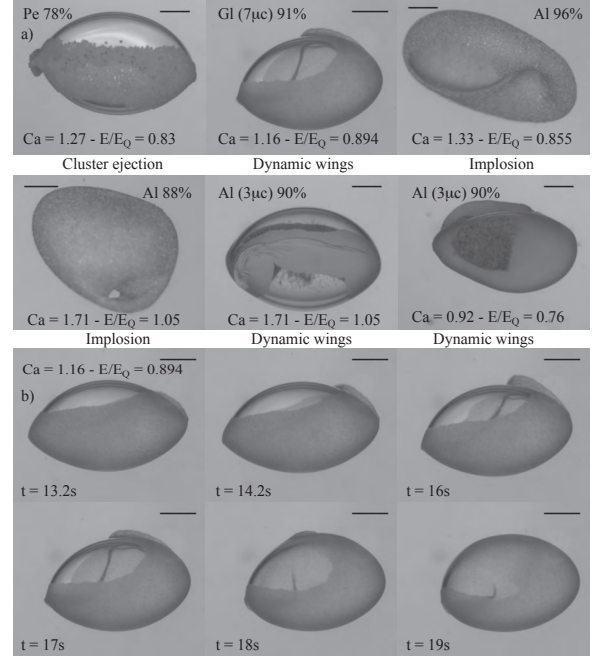


FIG. 8: (a) Drop behaviors for very strong electrical fields. (b) Evolution of the “dynamic wings”. The scale bar corresponds to 1 mm.

#### IV. DISCUSSION

In summary, our experiments show that surface-adsorbed particles suppress the electrohydrodynamic flow, enhance overall oblate drop deformation, and decrease the threshold for rotational flow. Modification of the surface properties, e.g., surface tension, interfacial viscoelasticity and surface conductivity, could be responsible for these effects. Here we discuss each of these mechanisms and show that the oblate deformation of the particle-covered drop is well captured by a capsule model; the colloidal membrane endows the interface with shear elasticity which immobilizes the interface and suppresses the flow. The decrease in the tilt threshold, however, can not be explained at this time with the available shell model [37, 41].

##### A. Modification of the surface tension

The increase of deformation could be related to a lower effective interfacial tension,  $\gamma_{eff}$ , due to the particles. Fitting the data on Figure 4 with the Taylor model Eq. 5 yields  $\gamma_{eff}$  in the range  $[0.12 - 0.16]$  mN/m, which corresponds to a decrease of almost 97% relative to the tension for the clean interface. Impact of surface absorbed particles on the surface tension has been studied in relation with Pickering emulsion and liquid marbles[42]. The presence of solid particles at the interface usually is associated reduction of the liquid/liquid interfacial tension [43, 44]. Theoretical modeling [45] shows that



for dense monolayer of mono-disperse spherical particles,  $\gamma_{eff}$  depends mainly on the contact angle of the particles,  $\gamma_{eff} = \gamma[1 - \pi(1 - \cos\theta)^2/4\sqrt{3}]$ , and shouldn't decrease below 50% of  $\gamma$ . This order of magnitude is confirmed by experimental measurement [43, 46]. For lower concentration of particles, almost no variation of  $\gamma$  were measured [47, 48]. Recent publications [44, 48] on marble liquids point out the strong dependence of  $\gamma_{eff}$  on size, concentration, surface free energy and water contact angle of the encapsulating powder. For non-densely packed particles, the capillary interactions between particles can be neglected, and the “modified” surface tension can be expressed as  $\gamma_{eff} = \gamma + (\gamma_{sl} + \gamma_{sa} - \gamma)A_0/A$  [48], where  $\gamma_{SL}$  and  $\gamma_{SA}$  are respectively the surface tension at the powder/liquid and powder/air interface, and  $A$  and  $A_0$  are the total surface of the marble and the surface covered by particles. Estimate for all drops considered in our work show that  $\gamma_{eff}$  should be relatively close to  $\gamma$ . Hence, a lower interfacial tension can not explain the strong increase of the drop deformation. Moreover,  $\gamma_{eff}$  should vary with the electrical fields, as the packing changes with the electrical fields leading to a non linear variation with the deformation. In conclusion, a variation of the interfacial tension due to the presence of surface-adsorbed particles can not explain the strong deformation increase compared to a clean drop.

### B. Surface conductivity

We can model the monolayer of surface-adsorbed particles as a solid shell, with an equivalent surface conductivity estimated as the particle conductivity divided by the particle diameter (which is a measure of the thickness particle monolayer),  $\sigma_s \sim \sigma_p/(2r)$ . The current conservation boundary condition may be expressed as (assuming negligible charge convection, which is reasonable in weak fields and small drop deformations)  $\sigma_{ex}E_n^{ex} - \sigma_{in}E_n^{in} = -\sigma_s \nabla_s \cdot \mathbf{E}_t$ . The solution shows that the deformation is described by the same discriminating function in the Taylor theory Eq. 5 but with  $R$  replaced by  $R + 2R_s$  where  $R_s = \sigma_s a / \sigma_{ex}$  is the dimensionless surface conductivity. This shows that oblate deformation should be suppressed as the particle conductivity increases and eventually the drop deformation should change from oblate to prolate. In our experiments however we observe enhancement of the oblate deformation by the surface-adsorbed particles, not suppression. This implies that surface conductivity is unlikely to play a significant role in drop deformation.

### C. Interfacial viscosity

Particles at interfaces behave as two-dimensional suspension. Accordingly, the increased dissipation arising from the particle motions results in increased surface viscosities [49–51]. A drop with high surface viscosities effectively acts as a drop with very high bulk viscosity. In

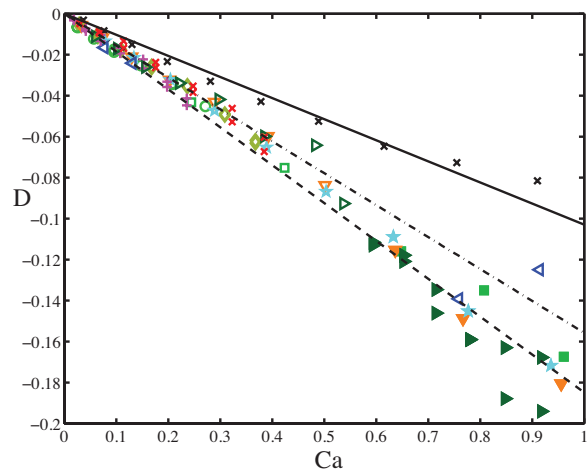


FIG. 9: Drop deformation as a function of the capillary number. Symbols the same as in Figure 4. The solid line represents the Taylor theory Eq. 5 for  $\lambda = 0.07$ , the dashed line is Eq. 8 for  $\lambda \rightarrow \infty$ , and the lines for capsule model Eq. 9 with shear elastic modulus  $1.43\gamma$ .

the limit of high viscosity ratio Taylor’s law gives

$$D = Ca \frac{9(-19 + (5 + 9R + 5R^2)S)}{80S(2 + R)^2} \quad (8)$$

Increased surface viscosity also suppresses the surface flow, see Eq. 4.

Figure 9 shows the comparison between the experimental data and the theoretical curve for an infinitely viscous drop Eq. 8. The theoretical curve is close to the data specially for low capillary numbers but still underestimates the measured deformation. Hence, the effect of the presence of particles can not be completely explained by the suppression of the electrohydrodynamic flow. Moreover, we also observe that drop deformation continues to increase even above the rotation threshold (see Figure 4) in contrast to the theoretical prediction for high-viscosity drops [40].

### D. Interfacial elasticity

A monolayer of densely packed particles at a liquid interface behaves similarly to an elastic sheet [52–56] and can support anisotropic stresses and strains: it buckles in uniaxial compression and cracks under tension. This solid-like behavior can be characterized in terms of Young’s modulus and Poisson ratio derived from simple theoretical considerations see [52, 54, 57]. Recent theoretical model [58] shows that presence of a significant interfacial shear elasticity (greater than the interfacial tension) and of a nonzero interfacial compression elasticity can cause drops to buckle. In our experiments, the particle layer also eventually exhibit buckling, see Figure 8, suggesting that the particle-coated drop behaves like a capsule (a drop enclosed by an elastic membrane).

The deformation of capsules in electric fields has been considered in only two studies [59, 60]. Ha and Yang [59] developed a small deformation theory similar to the one for a capsule in external linear flows [61]. Since the particles at the interface are closely packed, the monolayer of jammed particles can be much more easily sheared than compressed (compacted). Accordingly, the particle monolayer can be modeled as an incompressible two-dimensional material and drop deformation is given by (see Appendix for details)

$$D_{eq} = Ca_s \left[ \frac{27((1+R)^2 - 4/S)}{32(2+R)^2} \right] \quad Ca_s = \frac{\varepsilon_{ex} E_0^2 a}{G} = Ca \frac{\gamma}{G} \quad (9)$$

where  $G$  is the elastic shear modulus. Figure 9 show the data fit with  $\gamma/G = 0.7$ . The value of  $G$  is in reasonable agreement with value deduced from the Young's modulus of particle rafts [52].

### E. Threshold for drop tilt and electrorotation

To estimate the effects of the particle monolayer on the onset of electrorotation, we consider the spherical shell [37, 41]. We can model the particle-covered drop as a layered sphere with effective properties  $\varepsilon_p$  and  $\sigma_p$ . For a thin shell [62]

$$\varepsilon_s = \frac{\varepsilon_p \varepsilon_{in}}{\varepsilon_p + \delta \varepsilon_{in}}, \quad \sigma_s = \frac{\sigma_p \sigma_{in}}{\sigma_p + \delta \sigma_{in}}, \quad \delta = \frac{2r}{a} \ll 1 \quad (10)$$

where the shell thickness corresponds to the particle diameter  $2r$ . While  $S$  is less affected by the particles,  $R$  can be significantly changed due to the wide range of particle conductivities. For example, Eq. 10 shows that presence of a resistive (very low-conductivity) layer decreases  $R$  and thereby lowering the rotation threshold Eq. 7. However, since this decrease is also observed for conductive particles, surface conduction most likely not a relevant explanation. A possible explanation may be drop asphericity; prolate rigid ellipsoids do have lower threshold for electrorotation than spheres [63, 64]. This issue requires further examination both experimentally and theoretically.

## V. CONCLUSIONS

We experimentally study the effect of high concentration of surface-adsorbed particles on drop deformation in a uniform DC electrical field. The fluid system consists of a silicon oil drop suspended in castor oil, both very weakly conducting liquids. A broad range of particle sizes, conductivities, and shapes is explored. In weak electric fields, the presence of particles enhances the deformation compared to a particle-free (clean) drop and suppresses the electrohydrodynamic flow. Drop deformation is well described by a capsule model, which treats the particle monolayer as an elastic sheet. In

stronger fields, drops tilt due to the Quincke effect but the onset is significantly lowered compared to the clean drop. The decrease can not be explained with the existing spherical shell model and likely due to drop asphericity. Even stronger electrical fields give rise to more exotic behaviors as ephemeral dynamic wings or drops implosion. The similarity between the particle-covered drop and a capsule provides promising new insight into the impact of particles on interfacial dynamics. Our findings open questions ranging from understanding the fluid/solid transition that occur for high surface coverage to stability of Pickering emulsions. We hope our work will stimulate further research on the electrohydrodynamics of particles at interfaces.

## VI. ACKNOWLEDGEMENT

This research was supported by NSF awards CBET-1132614 and CBET-1437545.

### Appendix A: Small-deformation theory for an initially spherical elastic capsule placed in a uniform DC electric field

An uniform DC electric field,  $\mathbf{E} = E_0 \hat{\mathbf{z}}$ , exerts electric pressure and shear on a sphere with non-capacitive interface (continuous electric potential)[31]

$$\mathbf{t}^{\text{el}} = p^{\text{el}} (1 + 3 \cos 2\theta) \hat{\mathbf{r}} + \tau_s^{\text{el}} \sin 2\theta \hat{\boldsymbol{\theta}} \quad (\text{A1})$$

where

$$p^{\text{el}} = -\frac{3(R^2 + 1 - 2/S)}{4(R + 2)^2}, \quad \tau_s^{\text{el}} = \frac{9(R - 1/S)}{2(R + 2)^2}. \quad (\text{A2})$$

The electric tractions deforms the interface; the material particles at the interface move to new position described by

$$\mathbf{x}_s = a \left[ (1 + s(1 + 3 \cos 2\theta)) \hat{\mathbf{r}} + u \sin 2\theta \hat{\boldsymbol{\theta}} \right] \quad (\text{A3})$$

The in-plane displacement does not generate overall shape change but creates elastic stresses that oppose the electric shear and immobilize the interface. The deviation from sphericity is qualified by  $s$

$$D = 3s, \quad d_{||} = r_s(0) = 1 + 4s, \quad d_{\perp} = r_s(\pi/2) = 1 - 2s \quad (\text{A4})$$

For small deformations the membrane behaves as an elastic-Hookean material and the elastic stresses are [59, 60, 65]

$$\mathbf{t}^m = p^m (1 + 3 \cos 2\theta) \hat{\mathbf{r}} + \tau_s^m \sin 2\theta \hat{\boldsymbol{\theta}}, \quad (\text{A5})$$

where

$$\tau^m = 2(2Ca_s^{-1}u + 3Ca_a^{-1}(2s + u)) \quad p^m = 2Ca_a^{-1}(2s + u). \quad (\text{A6})$$

$Ca_s$  and  $Ca_a$  are the dimensionless shear and extensional elasticities;  $Ca_s = \varepsilon_{\text{ex}} E_0^2 a / G$ . Balancing the electric and elastic stresses, Eq. A1 and Eq. A5, yields

$$s = Ca_s \frac{\tau_s^{\text{el}}}{8} - (3Ca_s + 2Ca_a) \frac{p^{\text{el}}}{8} \quad (\text{A7})$$

In the limit of inextensible membrane,  $Ca_a \rightarrow 0$ , we obtain Eq. 9.

- 
- [1] Wu, N.; Russel, W. B. Micro- and nano-patterns created via electrohydrodynamic instabilities. *Nanotoday* **2009**, *4*, 180.
- [2] Wu, N.; Pease, L. F.; Russel, W. B. Electric-field-induced patterns in thin polymer films: Weakly nonlinear and fully nonlinear evolution. *Langmuir* **2005**, *21*, 12290–12302.
- [3] Roberts, S. A.; Kumar, S. AC electrohydrodynamic instabilities in thin liquid films. *J. Fluid Mech.* **2009**, *631*, 255–279.
- [4] Lin, T.; Rubinstein, S. M.; Korchev, A.; Weitz, D. A. Pattern Formation of Charged Particles in an Electric Field. *Langmuir* **2014**, *30*, 12119–12123.
- [5] de la Mora, J. F. The fluid dynamics of Taylor cones. *Ann. Rev. Fluid. Mech.* **2007**, *39*, 217–243.
- [6] Collins, R. T.; Jones, J. J.; Harris, M. T.; Basaran, O. A. Electrohydrodynamic tip streaming and emission of charged drops from liquid cones. *Nature Physics* **2008**, *4*, 149–154.
- [7] Xie, J.; Jiang, J.; Davoodi, P.; Srinivasan, M. P.; Wang, C.-H. Electrohydrodynamic atomization: A two-decade effort to produce and process micro-/nanoparticulate materials. *Chem. Eng. Sci.* **2015**, *125*, 32–57.
- [8] Farook, U.; Stride, E.; Edirisinghe, M. J. Preparation of suspensions of phospholipid-coated microbubbles by coaxial electrohydrodynamic atomization. *J. Royal Soc. Interfaces* **2009**, *6*, 271–277.
- [9] Mahaingam, S.; Meinders, M. B. J.; Edirisinghe, M. Formation, Stability, and Mechanical Properties of Bovine Serum Albumin Stabilized Air Bubbles Produced Using Coaxial Electrohydrodynamic Atomization. *Langmuir* **2014**, *30*, 6694–6703.
- [10] Lecuyer, S.; Ristenpart, W. D.; Vincent, O.; Stone, H. A. Electrohydrodynamic size stratification and flow separation of giant vesicles. *Applied Phys. Lett.* **2008**, *92*, 104105.
- [11] Vigo, C. R.; Ristenpart, W. D. Aggregation and Coalescence of Oil Droplets in Water via Electrohydrodynamic Flows. *Langmuir* **2010**, *26*, 10703–10707.
- [12] Ristenpart, W. D.; Jiang, P.; Slowik, M. A.; Punckt, C.; Saville, D. A.; Aksay, I. A. Electrohydrodynamic Flow and Colloidal Patterning near Inhomogeneities on Electrodes. *Langmuir* **2008**, *24*, 12172–12180.
- [13] Velev, O. D.; Gangwal, S.; Petsev, D. N. Particle-localized AC and DC manipulation and electrokinetics. *Annual Reports on the Progress of Chemistry Section C-Physical Chemistry* **2009**, *105*, 213–245.
- [14] Prieve, D. C.; Sides, P. J.; Wirth, C. L. 2-D assembly of colloidal particles on a planar electrode. *Current Opinion in Colloids and Interface Sci.* **2010**, *15*, 160–174.
- [15] van Blaaderen, A.; Dijkstra, M.; van Roij, R.; Imhof, A.; Kamp, M.; Kwaadgras, B. W.; Vissers, T.; Liu, B. Manipulating the self assembly of colloids in electric fields. *Eur. Phys. J -Special Topics* **2013**, *222*, 2895–2909.
- [16] Aranson, I. S. Collective behavior in out-of-equilibrium colloidal suspensions. *C. R. Physique* **2013**, *14*, 518–527.
- [17] Dobnikar, J.; Snezhko, A.; Yethiraj, A. Emergent colloidal dynamics in electromagnetic fields. *Soft Matter* **2013**, *9*, 3693–3704.
- [18] Woehl, T. J.; Chen, B. J.; Heatley, K. L.; Talken, N. H.; Bukosky, S. C.; Dutcher, C. S.; Ristenpart, W. D. Bifurcation in the Steady-State Height of Colloidal Particles near an Electrode in Oscillatory Electric Fields: Evidence for a Tertiary Potential Minimum. *Phys. Rev X* **2015**, *5*.
- [19] Brugarolas, T.; Tu, F.; Lee, D. Directed assembly of particles using microfluidic droplets and bubbles. *Soft Matter* **2013**, *9*, 9046–9058.
- [20] Furst, E. M. Directing colloidal assembly at fluid interfaces. *PNAS* **2011**, *108*, 20853–20855.
- [21] Cavallaro, M., Jr.; Botto, L.; Lewandowski, E. P.; Wang, M.; Stebe, K. J. Curvature-driven capillary migration and assembly of rod-like particles. *PNAS* **2011**, *108*, 20923–20928.
- [22] Cui, M.; Emrick, T.; Russell, T. P. Stabilizing Liquid Drops in Nonequilibrium Shapes by the Interfacial Jamming of Nanoparticles. *Science* **2013**, *342*, 460–463.
- [23] Dommersnes, P.; Rozynek, Z.; Mikkelsen, A.; Castberg, R.; Kjerstad, K.; Hersvik, K.; Fossum, J. Active structuring of colloidal armor on liquid drops. *Nature Communications* **2013**, *4*, 2066.
- [24] Ouriemi, M.; ; Vlahovska, P. M. Electrohydrodynamics of particle-covered drops. *J. Fluid Mech.* **2014**, *751*, 106–120.
- [25] Rozynek, Z.; Mikkelsen, A.; Dommersnes, P.; Fossum, J. O. Electroformation of Janus and patchy capsules. *Nature Comm.* **2014**, *5*.
- [26] Rozynek, Z.; Dommersnes, P.; Mikkelsen, A.; Michels, L.; Fossum, J. O. Electrohydrodynamic controlled assembly and fracturing of thin colloidal particle films confined at drop interfaces. *Eur. Phys. J. Special Topics* **2014**, *223*, 1859–1867.
- [27] Lanauze, J. A.; Walker, L. M.; Khair, A. S. The influence of inertia and charge relaxation on electrohydrodynamic drop deformation. *Phys. Fluids* **2013**, *25*.
- [28] Jones, T. B. *Electromechanics of particles*; Cambridge University Press: New York, 1995.
- [29] Melcher, J. R.; Taylor, G. I. Electrohydrodynamics - a review of role of interfacial shear stress. *Annu. Rev. Fluid Mech.* **1969**, *1*, 111–146.
- [30] Saville, D. A. Electrohydrodynamics: The Taylor-Melcher leaky dielectric model. *Annu. Rev. Fluid Mech.* **1997**, *29*, 27–64.
- [31] Taylor, G. I. Studies in electrohydrodynamics. I. Circulation produced in a drop by an electric field. *Proc. Royal Soc. A* **1966**, *291*, 159–166.
- [32] Ha, J. W.; Yang, S. M. Electrohydrodynamics and electrorotation of a drop with fluid less conductive than that



- of the ambient fluid. *Phys. Fluids* **2000**, *12*, 764–772.
- [33] Salipante, P. F.; Vlahovska, P. M. Electrohydrodynamics of drops in strong uniform DC electric fields. *Phys. Fluids* **2010**, *22*, 112110.
- [34] Sato, H.; Kaji, N.; Mochizuki, T.; Mori, Y. H. Behavior of oblatelly deformed droplets in an immiscible dielectric liquid under a steady and uniform electric field. *Phys. Fluids* **2006**, *18*, 127101.
- [35] Salipante, P. F.; Vlahovska, P. M. Electrohydrodynamic rotations of a viscous droplet. *Phys. Rev. E* **2013**, *88*, 043003.
- [36] Quincke, G. Ueber Rotation em im constanten electrischen Felde. *Ann. Phys. Chem.* **1896**, *59*, 417–86.
- [37] Jones, T. B. Quincke rotation of spheres. *IEEE Trans. Industry Appl.* **1984**, *20*, 845–849.
- [38] Turcu, I. Electric field induced rotation of spheres. *J. Phys. A: Math. Gen.* **1987**, *20*, 3301–3307.
- [39] Lemaire, E.; Lobry, L. Chaotic behavior in electro-rotation. *Physica A* **2002**, *314*, 663–671.
- [40] He, H.; Salipante, P. F.; Vlahovska, P. M. Electrorotation of a viscous droplet in a uniform direct current electric field. *Phys. Fluids* **2013**, *25*, 032106.
- [41] Turcu, I.; Lucaciu, C. M. Electrorotation -a spherical shell model. *J. Phys. A* **1989**, *22*, 995–1003.
- [42] Aussillous, P.; Quere, D. Liquid Marbles. *Nature* **2001**, *411*, 924–927.
- [43] Nushtaeva, A. V.; Kruglyakov, P. M. Investigation of Model Emulsion Films Stabilized by Solid Particles: Thickness of Films, Their Stability, and Interfacial Tension. *Colloid J.* **2004**, *66*, 456–465.
- [44] Cengiz, U.; Erbil, H. Y. The lifetime of floating liquid marbles: the influence of particle size and effective surface tension. *Soft Matter* **2013**, *9*, 8980.
- [45] Levine, S.; Bowen, B. D.; Patridge, S. J. Stabilization of emulsions by fine particles II. capillary and van der Waals forces between particles. *Colloids and Surfaces* **1989**, *38*, 345–364.
- [46] Vilkova, N. G.; Nushtaeva, A. V. Influence of hydrophobized solid particles on the reduction of interfacial tension. *Mendelev Commun* **2013**, *23*, 155–156.
- [47] Vignati, E.; Piazza, R.; P., L. T. Pickering Emulsions: Interfacial tension, colloidal layer morphology, and trapped-particles motion. *Langmuir* **2003**, *19*, 6650–6656.
- [48] Bormashenko, E.; Musin, A.; Whyman, G.; Barkay, Z.; Starostin, A.; Valtsifer, V.; Strelnikov, V. Revisiting the surface tension of liquid marbles: Measurement of the effective surface tension of liquid marbles with the pendant marble method. *Colloids Surfaces A* **2013**, *425*, 15–23.
- [49] Fuller, G. G.; Vermant, J. Complex Fluid-Fluid Interfaces: Rheology and Structure. *Annu. Rev. Chem. Biochem. Eng.* **2012**, *3*, 519–543.
- [50] Lishchuk, S. V.; Halliday, I. Effective surface viscosities of a particle-laden fluid interface. *Phys. Rev. E* **2009**, *80*, 016306.
- [51] Lishchuk, S. V. Effective surface dilatational viscosity of highly concentrated particle-laden interfaces. *Phys. Rev. E* **2014**, *90*, 053005.
- [52] Vella, D.; Aussillous, P.; Mahadevan, L. Elasticity of an interfacial particle raft. *Europhys. Lett.* **2004**, *68*, 212–218.
- [53] Pocivavsek, L.; Dellsy, R.; Kern, A.; Johnson, S.; Lin, B.; Lee, K. Y. C.; Cerda, E. Stress and fold localization in thin elastic membranes. *Science* **2008**, *320*, 912–916.
- [54] Planchette, C.; Lorenceau, E.; Biance, A.-L. Surface wave on a particle raft. *Soft Matter* **2012**, *8*, 2444–2451.
- [55] Xu, H.; Melle, S.; Golemanov, K.; Fuller, G. Shape and Buckling Transitions in Solid-Stabilized Drops. *Langmuir* **2005**, *21*, 10016–10020.
- [56] Datta, S. S.; Shum, H. C.; Weitz, D. A. Controlled Buckling and Crumpling of Nanoparticle-Coated Droplets. *Langmuir* **2010**, *26*, 18612–18616.
- [57] Cicuta, P.; Vella, D. Granular Character of Particle Rafts. *Phys. Rev. Lett.* **2009**, *102*, 138302.
- [58] Erni, P.; Jerri, H. A.; Wong, K.; Parker, A. Interfacial viscoelasticity controls buckling, wrinkling and arrest in emulsion drops undergoing mass transfer. *Soft Matter* **2012**, *8*, 6958–6957.
- [59] Ha, J. W.; Yang, S. M. Electrohydrodynamic effects on the deformation and orientation of a liquid capsule in a linear flow. *Phys. Fluids* **2000**, *12*, 1671–1684.
- [60] Karyappa, R. B.; Deshmukh, S. D.; Thaokar, R. M. Deformation of an elastic capsule in a uniform electric field. *Phys. Fluids* **2014**, *26*.
- [61] Barthes-Biesel, D.; Sgaier, H. Role of membrane viscosity in the orientation and deformation of a spherical capsule suspended in shear flow. *J. Fluid. Mech.* **1985**, *160*, 119–135.
- [62] Jones, T. B. Basic theory of dielectrophoresis and electrorotation. *IEEE Eng Med Biol Mag.* **2003**, *22*, 33–42.
- [63] Cebers, A.; Lemaire, E.; Lobry, L. Electrohydrodynamic instabilities and orientation of dielectric ellipsoids in low-conducting fluids. *Phys. Rev. E* **2000**, *63*, 016301.
- [64] Dolinsky, Y.; Elperin, T. Electrorotation of a leaky dielectric spheroid immersed in a viscous fluid. *Phys. Rev. E* **2009**, *80*, 066607.
- [65] Vlahovska, P. M.; Young, Y.-N.; Danker, G.; Misbah, C. Dynamics of a non-spherical microcapsule with incompressible interface in shear flow. *J. Fluid. Mech.* **2011**, *678*, 221–247.